JACS
JOURNAL OF THE AMERICAN CHEMICAL SOCIETY

Article

pubs.acs.org/JACS

Indentation and Self-Healing Mechanisms of a Self-Assembled Monolayer—A Combined Experimental and Modeling Study

Christian Meltzer,[†,‡] Jonas Paul,[†] Hanno Dietrich,[∥,⊥] Christof M. Jäger,[∥,¶] Timothy Clark,[∥] Dirk Zahn,[§,∥,⊥] Björn Braunschweig,[†,‡,§] and Wolfgang Peukert*[,†,‡,§]

[†]Institute of Particle Technology (LFG), Friedrich-Alexander-Universität Erlangen-Nürnberg (FAU), Cauerstrasse 4, 91058 Erlangen, Germany

[‡]Erlangen Graduate School in Advanced Optical Technologies (SAOT), Friedrich-Alexander-Universität Erlangen-Nürnberg (FAU), Paul-Gordan-Strasse 6, 91052 Erlangen, Germany

[§]Cluster of Excellence − Engineering of Advanced Material (EAM), Friedrich-Alexander-Universität Erlangen-Nürnberg (FAU), Nägelsbachstrasse 49b, 91052 Erlangen, Germany

[∥]Computer-Chemie-Centrum and Interdisciplinary Center for Molecular Materials and [⊥]Chair of Theoretical Chemistry, Friedrich-Alexander-Universität Erlangen-Nürnberg (FAU), Nägelsbachstrasse 25, 91052 Erlangen, Germany

Supporting Information

ABSTRACT: A combination of *in situ* vibrational sum-frequency generation (SFG) spectroscopy and molecular-dynamics (MD) simulations has allowed us to study the effects of indentation of self-assembled octadecylphosphonic acid (ODPA) monolayers on α-Al_2O_3(0001). Stress-induced changes in the vibrational signatures of C−H stretching vibrations in SFG spectra and the results of MD simulations provide clear evidence for an increase in *gauche*-defect density in the monolayer as a response to indentation. A stress-dependent analysis indicates that the defect density reaches saturation at approximately 155 MPa. After stress is released, the MD simulations show an almost instantaneous healing of pressure-induced defects in good agreement with experimental results. The lateral extent of the contact areas was studied with colocalized SFG spectroscopy and compared to theoretical predictions for pressure gradients from Hertzian contact theory. SFG experiments reveal a gradual increase in *gauche*-defect density with pressure before saturation close to the contact center. Furthermore, our MD simulations show a spatial anisotropy of pressure-induced effects within ODPA domains: molecules tilted in the direction of the pressure gradient increase in tilt angle while those on the opposite side form *gauche*-defects.

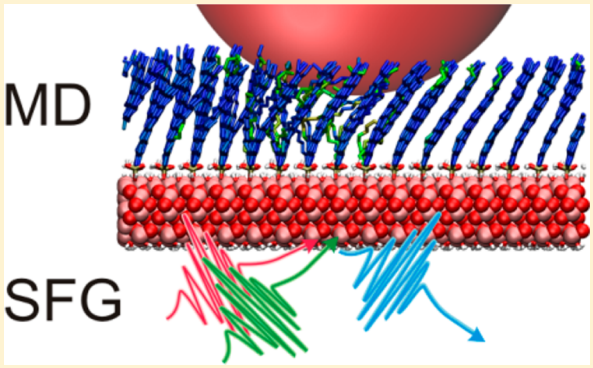

INTRODUCTION

Self-assembled monolayers (SAMs) serve as functional building blocks that tune the macroscopic properties of materials and devices. Examples are corrosion resistance and the performance in organic field-effect transistors, lubrication via physicochemical properties of the SAM, or particle properties.[1−8] Besides the choice of a suitable molecule that serves the needs of the desired application, the macroscopic functionality of a SAM is strongly influenced by the molecular structure of the monolayer.[9,10] Therefore, investigations of defect formation in monolayers is highly relevant for all potential applications of SAMs. In many cases mechanical stress is an external factor that influences the structure of molecular monolayers substantially and is thus likely to change the functionality of a SAM considerably. It is, for example, well-known in tribology that defects in a SAM strongly affect lubrication properties, making it possible to tailor frictional responses by tuning the molecular structure of a surface-adsorbed layer.[11−13] For that reason, molecular-level information on SAMs under pressure is of great importance and will help to increase molecular control of self-assembled monolayers under relevant conditions.

While the mechanism of defect formation in mechanically stressed SAMs is of great interest, the question of whether stress induced defects are self-healing or not is of equal importance. Several studies of SAMs under mechanical stress have been carried out using atomic-force microscopy (AFM), nanotribometry, or surface-force investigations that provide detailed structure−activity relations between lubrication properties and macroscopic or microscopic structures.[11,14−17] However, these experimental studies only provide limited information on the structural changes during and after release of applied mechanical stress. Molecular-dynamics (MD) simulations of thin molecular films under pressure and/or

Received: May 14, 2014
Published: July 11, 2014

   dx.doi.org/10.1021/ja5048076 | J. Am. Chem. Soc. 2014, 136, 10718−10727

shear are used to support and interpret these experiments providing additional information about structural changes of SAMs under mechanical stress.[18−24]

In contrast, vibrational spectroscopy can provide *in situ* access to information about the effects of mechanical stress on monolayers. In particular, nonlinear optical spectroscopic techniques such as second-harmonic generation (SHG) and sum-frequency generation (SFG) are well suited because of their inherent high sensitivity to surface species. However, these methods have so far been used only to a limited extent in tribological experiments which show that effects of mechanical indentation on SAMs strongly depend on the molecules that form the SAM, the intermolecular interaction and the binding to the substrate of the system studied.[25−33] Strongly decreasing SFG signals at an average pressure of 50 MPa exerted on a *n*-octadecyltriethoxysilane layer on crystalline quartz were related to the molecules lying flat on the crystal surface by Du et al.[32] While a full recovery of the SFG signal of these layers was observed after pressure release, indentation of zinc arachidate Langmuir−Blodgett films on sapphire has led to a noticeable transfer of molecules from the substrate to the indenter.[26,28,29] In addition to layer transfer and tilt angle changes, Berg and Klenermann needed to take the formation of *gauche*-defects (deviations of alkyl chain conformation from all-*trans*) into account to explain the observed changes in SFG signals in their study of alkyl thiols on gold. Obviously, from experiments useful information on the response of SAMs to mechanical pressure can be gained. The exact nature of the observed defects, e.g., where they are located within the alkyl chain remained, however, speculative. This lack of a mechanistic understanding of defect formation and their location can be closed by MD simulations which were previously performed for hydrocarbons on diamond and for thiols on Au.[22,23] However, so far experiments and simulations were performed on different systems. Obviously, only the combination of molecular-dynamics simulation with molecular level experiments is powerful enough to resolve defect formation and healing mechanisms.

To the best of our knowledge, only a few previous studies are available concerning self-healing mechanisms of pressure induced *gauche*-defects. Dlott and co-workers experimentally and theoretically studied the response of different SAMs on Au and Ag on laser driven shock waves revealing mainly elastic healing of defects on time scales of <100 ps.[34−36]

In this paper, we address molecular structure changes of octadecylphosphonic acid (ODPA) SAMs on α-Al_2O_3(0001) under mechanical stress and after stress release with a unique combination of colocalized SFG spectroscopy and MD simulations. Our approach has allowed us to experimentally monitor stress-induced changes *in situ* and compare these results with MD simulations, thus enabling us to obtain validated molecular level information on defect structures and on their distribution in great detail. Furthermore, the stability of our manipulation device and laser spectrometer allows us to apply defined loads and to probe contact areas *in situ* with SFG over hours without significant drift. This has allowed the first two-dimensional investigations of compressed SAMs and *gauche*-defect distributions within the entire contact area. In addition, the SAM was studied after pressure release revealing self-healing of induced defects. MD simulations furthermore provide insights on timescales of healing as well as healing mechanisms for different types of *gauche* defects.

Our results and conclusions are expected to have far-reaching implications for tuning functional properties of SAMs and creating an understanding of how different types of *gauche* defects return to all-*trans* conformation. Our methodology, the experimental approach and its combination with MD simulations, is of particular interest wherever molecular-scale defects between stressed solid bodies play a dominant role, such as for SAMs acting as lubricant or scratch resistant coatings for corrosion inhibition and in general for fundamental and applied aspects of adhesion, particle technology, and micromechanical systems.

THEORETICAL BACKGROUND AND METHODS

Sum-Frequency Generation (SFG). Vibrational SFG spectroscopy is a nonlinear optical technique that is sensitive to the vibrational modes of surface-adsorbed molecules. Infrared and visible pulsed laser beams of high intensity overlap spatially and temporally at the interface of interest and generate photons with frequencies equal to the sum of the fundamental frequencies of incident IR and visible beams. For a detailed discussion of the fundamentals of SFG the reader is referred to the Supporting Information and further literature;[37] here, only the details relevant for the interpretation of the experiments are discussed briefly.

The intensity of the sum-frequency signal is a combination of nonresonant contributions typically originating from the substrate and the resonant excitation of vibrations of interface molecules. In the case of α-Al_2O_3, nonresonant contributions are negligible.[38] In the dipole approximation, the vibrational bands are described with Lorentzian curves. The amplitude of the bands depends on the molecular number density of interfacial molecules and the orientational average of the hyperpolarizabilities of SFG-active molecules.[37] Thus, one finds the maximum SFG intensity for perfectly polar ordered molecular bonds, decreasing with a decrease in order. Furthermore, SFG signal vanishes for centrosymmetric systems.[37] Further details on the Lorentzian band shape and its dependencies are outlined in the Supporting Information.

The number density of SAMs with molecules strongly bound to the substrate can be considered constant for measurements under mechanical compression, so that intensity changes relate directly to changes in molecular order and orientation.

Experimental Setup. A custom-built broadband SFG spectrometer was used, which is described in further detail in the Supporting Information. Broadband IR pulses generated by the laser system allow measurements in the frequency range from 2750 to 3050 cm^{-1} without tuning the central IR wavelength. The IR beam is focused with a CaF_2 lens to a beam diameter of approximately 100 μm in the *y* and approximately 200 μm in the *x*-direction, determining the spatial resolution. Beam paths through the prism for our experimental setup are shown in Figure S1 in the Supporting Information. The self-assembled octadecylphosphonic acid monolayer was prepared on an α-Al_2O_3(0001) single crystal prism with a nanorough surface. Static contact angle measurements gave a contact angle of ∼102 ± 1° (based on 8 measurements on a 1 × 1 cm^2 sample) which is a value in the range typical for alkyl chain SAMs on α-Al_2O_3(0001).[39,40] The layer thickness was determined with the help of our phase modulated ellipsometer (Picometer Ellipsometer; Beaglehole Instruments; New Zealand) to be ∼2.2 nm. This corresponds to a tilt angle of roughly 30° based on an estimated length of the ODPA molecule of 2.4 nm. A normal force was exerted on the SAM with a custom-built manipulation device using a BK7 lens (radius 125 mm), generating a parabolic pressure distribution that induces mechanical stress to the SAM. Using atomic force microscopy, the rms roughness on an area of 2 μm × 2 μm of both the prism and the BK7 lens was determined to 0.24 and 0.37 nm, respectively. As the thickness of the monolayer is larger than the surface roughness, we can assume an intimate contact over almost the entire contact area.[29] This assumption is supported by the flattening of surface asperities.[32] Note that asperities could lead to local variations in contact pressure. However, considering the low

dx.doi.org/10.1021/ja5048076 | J. Am. Chem. Soc. 2014, 136, 10718−10727

surface roughness of substrate and indenter and the applied high loads, we can assume that the latter effect is negligible.[32] Therefore, it is valid to apply Hertzian contact theory in order to model the pressure distribution within the contact area.[41]

Details on the sample preparation, the manipulation device, the standard measurement procedure, and the Hertzian contact theory can be found in the Supporting Information.

Influence of the Experimental Geometry on the SFG Signal. Bringing lens and ODPA SAM in contact changes the linear optical properties for incident and SFG beams from the α-Al_2O_3/ODPA/air to the α-Al_2O_3/ODPA/BK7 interfaces. To take the corresponding change in reflection and transmission properties into account, an effective Fresnel coefficient F_{yyz} is introduced. A detailed discussion of F_{yyz} is given in the Supporting Information. Here we only present the results for the two relevant systems: with the BK7 lens not in contact, the Fresnel coefficient is $F_{yyz}^{air} = 1.3$ while it changes to $F_{yyz}^{BK7} = 4.6$ when contact is established. As a consequence, SFG amplitudes and intensities are enhanced by factors of 3.5 and 12.5, respectively, when the BK7 probe is in contact. The measured signals were corrected by these factors where applicable. A detailed discussion of where such a correction is possible is given below.

Molecular-Dynamics Simulations. Classical atomistic MD-simulations were carried out for ODPA SAMs on α-Al_2O_3(0001) analogously to previous work.[42] The surface represents the stable aluminum-terminated slab, which was hydroxylated in order to mimic the thermodynamically most favorable surface structure under ambient conditions.[43] Next, ODPA molecules were deposited onto the surface. Following the binding mechanism suggested by Bauer et al.,[43] singly deprotonated ODPA molecules replaced surface hydroxyl groups, to provide an electrostatically driven monodentate binding to the surface under water release.

To obtain an ordered SAM, the replacement of hydroxyl ions was carried out on a regular lattice. Two systems were prepared with ODPA densities of 3.80 and 5.07 molecules nm^{-2} to account for effects caused by different degrees of surface coverage. The densities lie at the upper and lower ends of the range of the experimentally[44,45] and theoretically[46] suggested surface coverage of alkyl-phosphonic acids on α-Al_2O_3. The force field was based on the Generalized Amber Force Field[47] and an aluminum oxide force field developed by Sun et al.[48] Further details on the systems and the force field can be found in the Supporting Information.

To model the effect of an indentation in the SAM, a repelling spherical potential with a radius r_0 was added to represent the curved surface of the lens as shown schematically in Figure 1. All atoms within the sphere ($\|\boldsymbol{r}_i - \boldsymbol{r}_{sph}\| < r_0$, with $\boldsymbol{r}_i$ and $\boldsymbol{r}_{sph}$ representing the position vectors of the atom and the sphere, respectively) experience a repelling potential which was chosen to increase harmonically from zero at the sphere's surface toward the center of the sphere. To simulate the indentation, a constant force F_p was applied to the sphere and it was allowed to move up or down, as depicted in Figure 1. For details on the indenting sphere, please consult the Supporting Information.

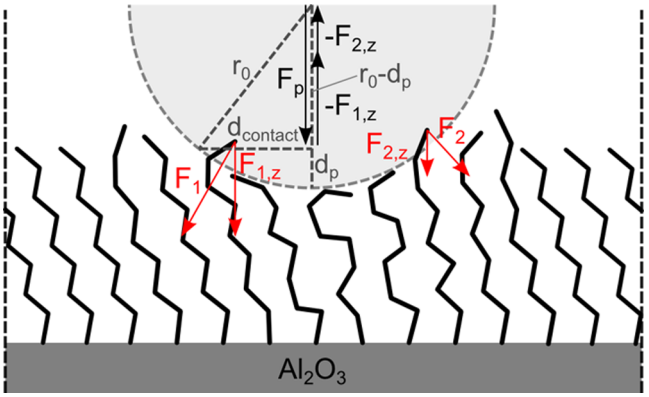

Figure 1. Schematic representation of the working principle of the MD simulations in equilibrium ($\boldsymbol{F}_p = -\Sigma \boldsymbol{F}_{i,z}$). The indenting sphere is shown in light gray. Periodic boundary conditions are illustrated by dashed lines at the sides.

All simulations were carried out using the DL_POLY Classic 1.9 code with slight modifications to introduce the repelling sphere.[49,50] The simulations were performed *in vacuo* at 300 K with 2D-periodic boundary conditions, a Berendsen thermostat,[51] and a leapfrog integrator. The integration time step was set to 1 fs and a cutoff radius of 12 Å was chosen for all nonbonding interactions. After equilibration, the simulations were run for 5 ns. Snapshots for analysis were taken every picosecond to obtain a statistically relevant amount of data.

Two different sphere radii of 30 and 60 Å were used to investigate the influence of the curvature of the sphere. The results were compared to simulations without pressure. A summary of the various systems and their key parameters is given in Table 1.

Table 1. Surface Coverage c, Sphere Radius r_0, Approximate Stress σ, and Corresponding Force F_p

	c [nm^{-2}]	r_0 [Å]	σ [MPa]	F_p [nN]
$MD^{pristine}_{3.80/nm^2}$	3.80	-	-	-
$MD^{200\ MPa}_{3.80/nm^2}$	3.80	30	200	5.65
$MD^{500\ MPa}_{3.80/nm^2}$	3.80	30	500	14.14
$MD^{pristine}_{5.07/nm^2}$	5.07	-	-	-
$MD^{200\ MPa}_{5.07/nm^2}$	5.07	30	200	5.65
$MD^{500\ MPa}_{5.07/nm^2}$	5.07	30	500	14.14

RESULTS AND DISCUSSION

Effects of Mechanical Compression on ODPA. Figure 2a shows a representative SFG spectrum of a freshly prepared ODPA SAM, the spectrum is dominated by vibrational bands centered at 2880 and 2945 cm^{-1}. The former can be attributed to symmetric CH_3 stretching vibrations (CH_3^{ss}) of terminal methyl groups while the latter has been assigned to a superposition of methyl Fermi resonance (CH_3^F, 2942 cm^{-1}) and antisymmetric methyl stretching vibration (CH_3^{as}, 2965 cm^{-1}).[37,52]

SFG spectra of freshly prepared ODPA SAMs have negligible contributions from methylene groups, because of local inversion symmetry within perfectly aligned ODPA molecules. Here, all molecules are on average in an all-*trans* conformation with dihedral angles of 180°. Fitting the spectrum in Figure 2a as outlined in the Supporting Information yields an amplitude ratio of symmetric methylene stretching vibrations (CH_2^{ss}, 2852 cm^{-1}) to CH_3^{ss} (2880 cm^{-1}) of 0.10. This value is typical and was previously reported to be indicative of well-ordered ODPA SAMs.[37,53] All vibrational bands considered in our fitting procedures and their assignments are summarized in the Supporting Information.

Our analysis of pressure-induced changes was restricted to vibrational bands between 2800 and 2900 cm^{-1} because this spectral region contains the two most prominent modes CH_3^{ss} and CH_2^{ss}, which serve as excellent indicators for changes in molecular order. Analysis of the features located between 2900 and 2975 cm^{-1} is less informative.

The spectrum of the ODPA SAM under a load of 174 MPa is shown in Figure 2b. To account for changes in effective Fresnel coefficients once the lens is in contact, the measured SFG intensity is divided by a factor of 12.5 as discussed in the previous section. A close comparison of SFG spectra of unperturbed SAMs in Figure 2a and compressed SAMs with a mechanical stress of 174 MPa in Figure 2b reveals four distinct

dx.doi.org/10.1021/ja5048076 | J. Am. Chem. Soc. 2014, 136, 10718−10727

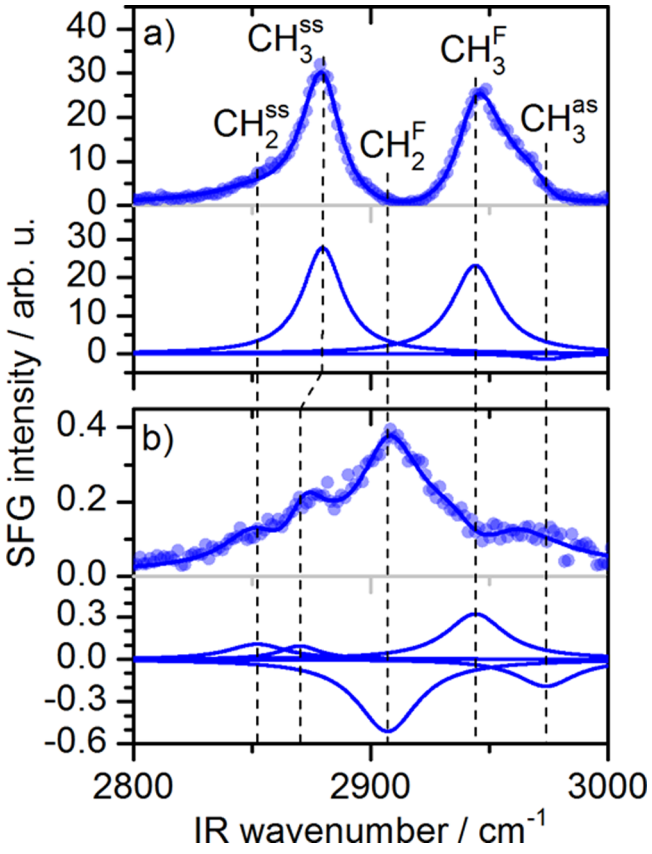

Figure 2. SFG spectra of ODPA SAMs on α-Al_2O_3(0001). (a) SFG spectrum of a freshly prepared SAM in air. (b) ODPA SAM under 174 MPa local pressure that was applied with a BK7 lens. Solid lines in the upper graphs are fits to experimental data (Supporting Information). Individual contributions are shown below each spectrum (negative contributions relate to a phase difference of π).

and substantial stress-induced changes: (i) The intensity of the CH_3^{ss} band decreases dramatically by ~99.3%. (ii) In addition, CH_3^{ss} red-shifts from 2880 cm^{-1} for the fresh SAM to 2870 cm^{-1}. (iii) A third band centered at 2852 cm^{-1} (CH_2^{ss}) appears. (iv) This third band is accompanied by a strong increase in intensity around 2907 cm^{-1} caused by contributions of a Fermi resonance of methylene symmetric stretching vibrations and the overtone of methylene bending vibrations (CH_2^F).

These observations become even clearer when the spectra are fitted based on Lorentzian band shapes. The amplitude of the CH_3^{ss} vibration is reduced by ~94%, while there is an almost 16-fold increase in CH_2^{ss}/CH_3^{ss} amplitude ratio.

The increase in CH_2^{ss}/CH_3^{ss} amplitude ratio is an excellent qualitative measure for stress-induced generation of *gauche*-defects because a pristine layer gives rise to negligible CH_2 contributions. An increase in the SFG intensities of CH_2 bands can be caused by local breaks in inversion symmetry of methylene groups[54] and thus by an induced change of dihedral angles of CH_2 groups caused by the formation of *gauche*-defects. The latter not only lift the local inversion symmetry of the CH_2 groups, but also change the orientations of CH_3 groups in directly affected and adjacent molecules.[37] These changes result in an overall decrease in orientational order and thus lead to a decrease in the average *z*-components of interfacial dipoles, causing SFG intensities to decrease substantially (Figure 2). Accordingly, the relative amplitudes of CH_2 and CH_3 vibrations are a good qualitative measure for the number density of *gauche*-defects.[55,56] The strong increase of their ratio during pressure loading thus clearly indicates that *gauche*-defects are being created as a response to external mechanical stress.

However, changes in the tilt angles of ODPA could also result in a decreased SFG intensity. Then, the tilt angle α_{tilt} of ODPA molecules would have to change from 30° for a closely packed and defect free SAM on α-Al_2O_3[46,57] to about 80° in order to account for the observed reduction in SFG intensity of ~99.4% (Figures 2 and 5).[29,58] Such a huge increase in tilt angle is highly unlikely due to steric hindrance for the required loss of specific volume.[30]

Deformation of alkyl chains in the compressed SAM also causes a substantial increase in SFG intensity of the CH_2 Fermi resonance centered at 2907 cm^{-1}. In an all-*trans* conformation the hydrogen atoms of CH_2 groups lie in a plane perpendicular to the plane of incidence. For ssp polarization, only vibrational components parallel to the plane of incidence contribute to SFG signals (see Supporting Information). Therefore, bending (scissoring) vibrations cannot be excited. Besides lifting CH_2 group inversion symmetry, pressure-induced defects rotate CH_2 groups and render the bending vibration SFG active for the polarization combination used in this study. This results in excitations of the Fermi resonance from the overtone of the methylene bending mode as well as the methylene symmetric stretching vibration. The strength of this feature as observed in Figure 2b indicates strong deformation of the alkyl chains and is in excellent agreement with the change of CH_2^{ss}/CH_3^{ss} amplitude ratio. Observations of CH_2^F vibrations from alkyl chains by using p- and s-polarized IR beams are reported in the

Table 2. *z*-Component of Bond Vectors Averaged over All CH_2 ($l_{z,CH2}$) and CH_3 ($l_{z,CH3}$) Groups, Respectively, within a Cylindrical Volume of 15 Å Radius around the Center, α_{tilt} Average over All Molecules in the Same Volume, Gauche Defect Density ρ_{gauche}, Penetration Depth d_p, and Corresponding Diameter $d_{contact} = 2(r_0^2 - (r_0 - d_p)^2)^{1/2}$ of the Contact Area (cf. Figure 1)[b]

	$l_{z,CH2}$ [a.u./nm^2]	$l_{z,CH3}$ [a.u./nm^2]	$(l_{CH_2,z}/l_{CH_3,z})$	ρ_{gauche}[a] [1/nm^2]	α_{tilt} [°]	d_p [Å]	$d_{contact}$ [Å]
$MD^{pristine}_{3.80/nm^2}$	1.47 ± 0.30	2.91 ± 0.17	0.51	0.85 ± 0.42	39.9 ± 0.4	---	---
$MD^{200\ MPa}_{3.80/nm^2}$	4.51 ± 0.63	0.69 ± 0.12	6.50	5.38 ± 0.66	37.8 ± 0.3	6.3	18.4
$MD^{500\ MPa}_{3.80/nm^2}$	4.46 ± 0.58	0.43 ± 0.09	10.43	7.43 ± 0.44	49.9 ± 0.5	11.4	35.2
$MD^{pristine}_{5.07/nm^2}$	0.59 ± 0.13	4.22 ± 0.20	0.14	0.13 ± 0.14	4.5 ± 0.4	---	---
$MD^{200\ MPa}_{5.07/nm^2}$	5.05 ± 0.56	1.66 ± 0.22	3.04	9.51 ± 1.14	13.2 ± 0.7	5.1	16.7
$MD^{500\ MPa}_{5.07/nm^2}$	4.29 ± 0.64	1.28 ± 0.16	4.93	13.21 ± 0.72	20.6 ± 0.5	15.0	39.6

[a]Number of dihedral angles in alkyl chain lower than 120°. [b]Averages and standard deviation were calculated from 5000 individual frames per simulation.

dx.doi.org/10.1021/ja5048076 | J. Am. Chem. Soc. 2014, 136, 10718−10727

existing literature[59,60] where an increase of CH_2^F spectral contribution with conformational disorder is clearly observed and is in accordance with our observations.

The stress-induced red-shift of CH_3^{ss} bands can be attributed to an increased dampening of the oscillator strength due to compression of the SAM. This effect is comparable to red-shifts of CH_3 bands from alkyl SAMs in air and under certain solvents,[61,62] although the magnitude of the shift due to compression is much stronger.

The interpretation of our experimental data regarding stress-induced changes in SAM structure is supported by the results from our MD simulations, as shown in Table 2. Here, pristine SAMs show a high degree of order with the low density SAM having a considerably higher tilt angle of 39.9° in comparison to 4.5° for the densely packed layer. Compressing perturbs the molecular order in the contact area for all the systems studied. The average *z*-components of the CH_2 and CH_3 bond vectors increase and decrease, respectively, as a response to the external pressure (Table 2) in accordance with our analysis of SFG spectra. The molecules below the simulated lens are kinked and twisted, as shown for an exemplary snapshot in Figure 3.

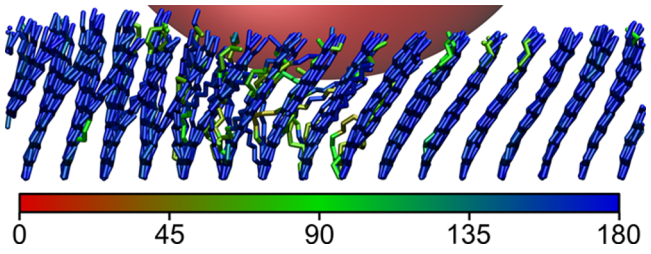

Figure 3. Side view along the *x*-axis on a snapshot in system $MD_{3.8/nm^2}^{200\ MPa}$ with only the carbon chains displayed and color coded according to the minimum backbone dihedral angle. The harmonic potential sphere is illustrated in red.

The penetration depths and surface area diameters listed in Table 2 vary depending on the applied force, the radius of the potential sphere, and the SAM density. As expected, the penetration depth is lower for the denser SAMs and for lower pressures (Table 2).

We have carried out a geometric analysis of CH_2 and CH_3 bond vectors and their *z*-components in order to compare the results of the MD simulations to those of the SFG experiments. As mentioned above, SFG signals are sensitive to cancellation of vibrations due to inversion symmetry. To analyze this cancellation effect, we calculated the CH_2 vibration vectors from the bond vectors for all 5000 simulation frames and eliminated inversion symmetric vectors by an iterative procedure outlined in the Supporting Information. By averaging the *z*-components of the remaining CH bond vectors over all CH_2 and CH_3 groups within a cylindrical volume in the affected area, we obtain an indication of the dipole moment derivatives of vibrations in the *z*-direction (because the dipole moment components arise mainly from the C-H bonds), and hence a qualitative description of SFG signal strengths.

Figure S4 in the Supporting Information depicts normalized CH_2 vibration vectors calculated from one MD frame for the unperturbed system $MD_{3.8/nm^2}^{pristine}$ and the perturbed one $MD_{3.8/nm^2}^{200\ MPa}$ before and after cancellation of inversion symmetric modes. The unperturbed system $MD_{3.8/nm^2}^{pristine}$ shows a very narrow distribution of vibration vectors in comparison to the highly spread distribution in the stressed system $MD_{3.8/nm^2}^{200\ MPa}$. After cancellation of the inversion-symmetric modes, the remaining vectors can be seen in both systems. However, the number and deviation from the *xy*-plane are significantly higher for the simulation of the stressed SAM.

Generally, the CH_2 groups lie more or less in the *xy*-plane for stretched, relaxed molecules as in the pristine SAMs $MD_{3.80/nm^2}^{pristine}$ and $MD_{5.07/nm^2}^{pristine}$. Hence, the dipole moment of the symmetrical CH_2 vibrations perpendicular to the surface (*z*-direction) is expected to be comparatively small in these two systems. For the lower density SAM, the value should be somewhat larger because of the higher tilt angle. The compressed systems can, however, be expected to have a stronger average dipole moment in *z*-direction because of *gauche*-defects and increased tilting.

In contrast to the methylene groups, the CH_3 groups face upward in the pristine ODPA-SAMs. Thus, the *z*-components of the bond vectors are almost as large as they can be and yield a strong dipole moment in the *z*-direction. In the systems with a repelling sphere, however, terminal CH_3 groups are often pressed flat in the *xy*-plane, which gives reason to expect a significant decrease in the dipole moment in the *z*-direction for the symmetric CH_3 vibrations.

As can be seen from the time-averaged values $l_{z,CH2}$ and $l_{z,CH3}$ shown in Table 2, the qualitative results match the expected behavior and therefore support our interpretation of the experimental results. All compressed systems show an increase in the average *z*-component of the CH_2 bond vectors by a factor of 3 ($MD_{3.80/nm^2}^{500\ MPa}$) to 11 ($MD_{5.07/nm^2}^{500\ MPa}$) and a significant decrease of 61% ($MD_{5.07/nm^2}^{200\ MPa}$) to 85% ($MD_{3.80/nm^2}^{200\ MPa}$) in the average *z*-component of the CH_3 bond vectors within the contact area relative to the pristine SAMs. Consequently, the CH_2/CH_3 ratio rises by a factor of ~35 within the contact area providing further evidence for the generation of *gauche*-defects.

Despite our cancellation procedure, a significant number of CH_2 vectors remains even for the pristine system. This can be attributed to an odd−even effect, since the molecules only contain 17 CH_2 groups so that one remains unpaired in well-ordered SAMs, but is not visible in the SFG spectra, because in the experiments the domain size is considerably smaller than the laser focus and thus the SFG intensity is an average over multiple domains which are all tilted in different directions.

To test this hypothesis, the molecular order in the system was investigated using the dihedral angles in the alkyl chains. In Figure 4, histograms of the dihedral angles in the alkyl chains are shown for three different systems with 3.8 molecules per square nanometer and are fitted to a Gaussian distribution. The region from 0° to 120° can be taken as a measure for the number of gauche defects. The pristine system consists of stretched chains and thus shows very few gauche defects, mainly in the terminal region of the alkyl chains. By contrast, the perturbed systems comprise a significant number of C−C bonds with dihedral angles of less than 120° indicating a high *gauche*-defect density. In Table 2, the time averaged density of *gauche*-defects is given. A comparison of these values with the corresponding CH_2 signal intensity reveals the correlation between these two variables: A higher defect density leads to a stronger CH_2 signal intensity.

This brings up the question of whether an increase in tilt angle or *gauche*-defect density dominates the changes in SFG signals. Taking into account the time-averaged change in tilt angles from our simulations (Table 2) we can calculate the change in SFG signals. The tilt angle change from our simulation would result in a decrease in SFG intensity of

dx.doi.org/10.1021/ja5048076 | J. Am. Chem. Soc. 2014, 136, 10718−10727

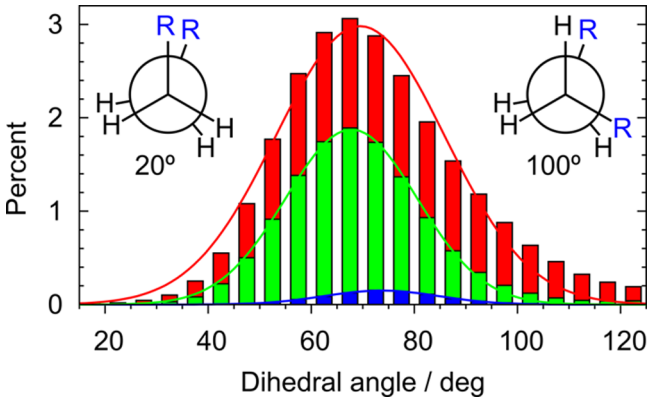

Figure 4. A Histogram of dihedral angles in the *gauche*-region for simulations with pristine $MD^{pristine}_{3.80/nm^2}$ (bottom, blue) and perturbed SAMs ($MD^{200\ MPa}_{3.80/nm^2}$ (middle, green) and $MD^{500\ MPa}_{3.80/nm^2}$ (top, red)) within 15 Å from the center of interaction. The lines depict fits with Gaussian curves.

approximately 1% and 36% for SAMs with high and low density, respectively.[29,58] These changes are inconsistent with the observed decrease of 99.3% in our SFG experiments with a SAM density in between those of the simulations[45,46] and further corroborate the above hypothesis that *gauche*-defects drive the change in SFG spectra.

Stress Dependence. Changes in the CH_2^{ss}/CH_3^{ss} ratio of SFG amplitudes and changes of the two individual amplitudes over a complete loading–unloading cycle are shown in Figure 5. The amplitudes were obtained from spectra measured at the center of the contact area. Here, the applied local pressure corresponds directly to a maximum in the Hertzian pressure distribution and thus serves as a direct measure for the applied stress. SFG amplitudes can be corrected easily for changes in effective Fresnel coefficients (see above). Applying a pressure to an ODPA SAM results in a sharp increase in the CH_2^{ss}/CH_3^{ss} ratio until a local maximum that is 19.4-fold higher than the value of a freshly prepared SAM is reached at 188 MPa. A subsequent increase in pressure to a maximum of 210 MPa leads to a decrease in the amplitude ratio, which is 12.1-fold higher than that of the pristine SAM (Figure 5). After unloading from the maximum pressure to 188 MPa, the CH_2^{ss}/CH_3^{ss} ratio increases again. For an interpretation of these changes, the pressure dependence of CH_2^{ss} and CH_3^{ss} amplitudes is analyzed separately: CH_3^{ss} amplitudes in Figure 5 show negligible pressure dependence once the pressure exceeds ~155 MPa. This is in good agreement with the observations from spatially resolved spectra, in which approximately the same minimum pressure is needed to drive CH_3^{ss} amplitudes to saturation, so that they become sample position independent close to the contact center (see Supporting Information). CH_3^{ss} amplitudes depend on the average *z*-component of methylene groups. Thus saturation indicates a local maximum in *gauche*-defect density, which remains unchanged until the maximum pressure of 210 MPa is applied. This observation indicates a stationary condition of the SAM at which no additional *gauche*-defects are induced and a limited level of molecular order is sustained. Within this pressure zone, CH_2^{ss} amplitudes decrease slightly, resulting in the decrease of CH_2^{ss}/CH_3^{ss} ratio, indicative of a slight reduction of the average *z*-component from SFG active methylene groups.

After pressure is released, self-healing of stress induced defects is observed: the CH_2^{ss}/CH_3^{ss} amplitude ratio decreases to

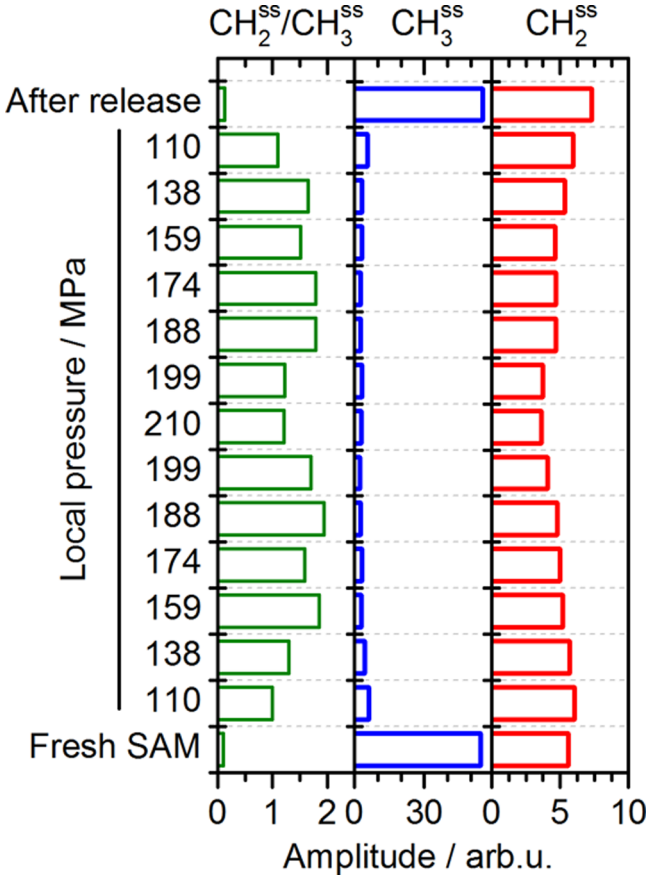

Figure 5. Changes in CH_2^{ss}/CH_3^{ss} amplitude ratio and the CH_2^{ss} and CH_3^{ss} amplitudes at the center of the contact area for a loading/unloading cycle. The amplitudes measured during contact are corrected by a factor of 3.5 that accounts for changes in effective Fresnel coefficients. Local pressures indicated on the *y*-axis are maximum pressures applied at the contact center based on Hertzian contact theory (Supporting Information).

0.13 which is comparable to the level of freshly prepared SAM (Figure 5). The latter is mainly caused by an increase of CH_3^{ss} amplitude to the level prior to compression, while for CH_2^{ss} a slightly higher value compared to a pristine SAM is established.

Therefore, we conclude that the majority of stress-induced defects of ODPA bound to a α-Al_2O_3(0001) substrate is completely reversible within the time scale (<1 s) that is accessible by our SFG spectrometer. Additionally the latter observations also show that a layer transfer from the α-Al_2O_3 (0001) surface to the BK7 lens is not observed. This can be explained by the high adsorption energy of ~178 kJ/mol of phosphonic acids on aluminum oxides.[43,63]

This conclusion from our experimental results is corroborated by MD simulations, in which the relaxation of the two systems with 500 MPa pressure, $MD^{500\ MPa}_{3.80/nm^2}$ and $MD^{500\ MPa}_{5.07/nm^2}$, was investigated after removal of the indenting sphere. At a temperature of 300 K, the CH_3 signal intensity reaches the original value with a half-life period of just 72 and 21 ps for the low and high density SAM, respectively (cf. Supporting Information Figure S12). The relaxation of the CH_2 signal and the *gauche*-defect density takes somewhat longer but still occurs with half-life periods of 119 and 36 ps, respectively. These timescales are well in line with ultrafast shock-compression experiments performed by Dlott and co-workers,[34−36] where a recovery within a time scale of 100 ps of

dx.doi.org/10.1021/ja5048076 | J. Am. Chem. Soc. 2014, 136, 10718−10727

shock-induced defects in alkane thiols on gold surfaces is observed.

It becomes obvious from the trajectories of the relaxation processes that the healing of *gauche*-defects takes place from the rim of the contact area toward its center, practically via a direct inversion of the indentation process. This can be seen nicely in Figures S14 and S15 of the Supporting Information.

In general, two mechanisms are conceivable for the generation and relaxation of *gauche*-defects: The first and most obvious is the generation or healing of a single defect, where the entire chain must rotate. This, however, mostly requires a large part of the molecule to be capable of rotating freely, which is rarely the case in SAMs. The second mechanism is the concerted generation of *gauche*-defects separated by one bond. In this mechanism, the overall molecular tilt is essentially conserved and only two atoms switch positions, as illustrated in Figure S13 in the Supporting Information.

Approximately 10% to 20% of the *gauche*-defects are produced and healed via the second mechanism. While the generation and healing of single defects occurs mainly for the head groups of ODPA, where the chains are not as constrained as in the bulk SAM. The double generation/healing mechanism dominates in the anchor region.

Comparing the relaxation times of both systems, it might seem contradictory that the more densely packed system relaxes much faster. The main reason for this is most certainly the positions of *gauche* defects in the molecules. In the lower density system, the chains at the rim of the contact region have ample space to tilt. However, as they are anchored below the repressing sphere, most of them need to kink, which in most cases happens near the anchor group. These low lying defects travel through the chain from the bottom to the top and thus the time required to heal these defects is higher compared to the densely packed $MD^{500\ MPa}_{5.07/nm^2}$ SAM. Here, the molecules cannot tilt to the side and thus form shallow *gauche*-defects that are located predominantly in the upper part of the alkyl chain where they can relax considerably faster. That is because a smaller part of the molecule must undergo a conformational change.

Lateral Extent of the Contact Area. As described in the Supporting Information, the force manipulator causes a parabolic pressure distribution when a normal force is applied. It is therefore interesting to investigate the lateral extent of the contact region and changes induced in the ODPA SAMs with colocalized SFG spectroscopy. For this purpose, the focus of the laser beam is scanned in *x*- and *y*-directions through the contact region and two-dimensional spatially resolved SFG spectra are recorded. Reliable simultaneous fitting of >1000 spectra per colocalized scan was not feasible; therefore, mean intensities for CH_3^{ss} (between 2868 and 2880 cm^{-1}) and CH_2^{ss} bands (between 2848 and 2856 cm^{-1}) instead of vibrational amplitudes are used for data analysis. Figure 6a shows laterally resolved CH_3^{ss} intensities at an applied normal force of 140 N (maximum pressure: 210 MPa). Comparison of changes in CH_3^{ss} intensity with the theoretical edge of the contact area according to Hertzian theory shows a strong decrease of CH_3^{ss} contributions toward the center of the contact which is consistent with the observations described above.

At the outer edge of the contact area, there is a 2-fold increase in CH_3^{ss} intensity compared to a pristine SAM. At this point, we recall our analysis of Fresnel coefficients that actually predicts an increase in SFG intensity once contact between probe and substrate is established and no molecular structure

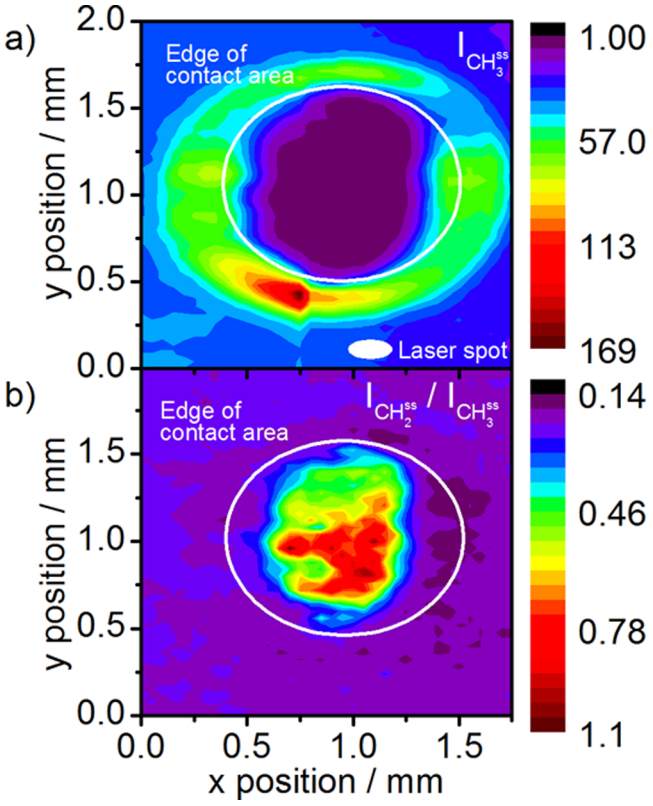

Figure 6. Two-dimensional colocalized SFG of the contact area between a BK7 lens and an ODPA SAM on α-Al_2O_3(0001). The applied normal force was 140 N which corresponds to a maximum pressure of 210 MPa at the contact center. (a) Position dependent change of CH_3^{ss} intensities in a.u. and the lateral dimension of the laser beam are shown for comparison. (b) The CH_2^{ss}/CH_3^{ss} intensity ratio. White solid lines correspond to the theoretical edge of the contact area according to Hertzian theory.

changes occur. An increase outside of the contact area is caused by changes in Fresnel coefficients with the lens being close enough to the SAM to change optical properties but not touching the SAM and thus preserving SAM structure. Within this transition area between purely Fresnel coefficient and additional molecular structure driven changes in SFG signals, the effective Fresnel factor gradually increases from F^{air}_{yyz} = 1.3 to F^{BK7}_{yyz} = 4.6. As both the boundaries of this region and the dependence of the Fresnel coefficients on the position within this region are not clearly defined, a Fresnel correction of the two-dimensional scans would lead to arbitrary changes in the results. Therefore, Fresnel coefficients are not taken into account for the lateral scans presented here.

To achieve comparison of theoretical and experimental contact area size independent of the Fresnel coefficient, CH_2^{ss}/CH_3^{ss} intensity ratios are plotted in Figure 6b. In contrast to Figure 6a deviations of CH_2^{ss}/CH_3^{ss} from the value of freshly prepared SAMs are limited to an area within the contact between lens and SAM. Therefore, significant amounts of *gauche*-defects are generated only within the direct contact area. To allow a detailed comparison of Hertzian pressure distribution and spatially resolved CH_2^{ss}/CH_3^{ss} Figure 7a–c shows scans through the contact area in *y*-direction and the corresponding pressure distribution for different normal forces. SFG spectra recorded for such a *y*-scan at a normal force of 140 N with a spatial resolution of 40 μm are shown in Figure 7d. Outside of the contact, SFG spectra exhibit typical features of a

dx.doi.org/10.1021/ja5048076 | J. Am. Chem. Soc. 2014, 136, 10718–10727

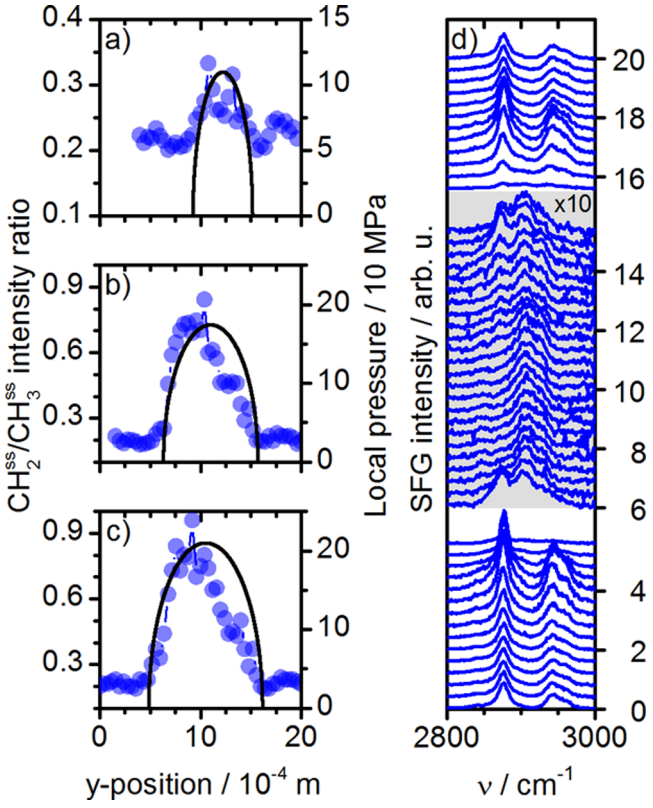

Figure 7. (a–c) Comparison of CH_2^{ss}/CH_3^{ss} intensity ratio (blue dots) and Hertzian pressure distribution (black lines) for applied normal forces as a function of *y*-position. Applied forces and the corresponding maximum pressures were (a) 20 N (110 MPa), (b) 80 N (174 MPa), and (c) 140 N (210 MPa). (d) Co-localized SFG spectra of an ODPA SAM on α-Al_2O_3(0001) at an applied normal force of 140 N (pressure at contact center 210 MPa). The SFG-focus region was scanned laterally through the contact area. The position axis on the right-hand side is given in 10^{-4} m units. The spectra shown on a gray background are multiplied by a factor of 10 in order to make the changes more apparent.

well-ordered SAM outlined above. When approaching the contact area, intensity rises due to changes in Fresnel coefficients without significant changes of the SFG spectrum. Inside the contact, CH_2^{ss} and CH_2^{F} contributions dominate the spectra. This is also apparent in the development of CH_2^{ss}/CH_3^{ss} for these spectra shown in Figure 7c. From the edge of the contact area, CH_2^{ss}/CH_3^{ss} rises almost linearly from approximately 0.2 to approximately 0.8 close to its center. A reduced normal force of 80 N changes the behavior only slightly with a maximum of CH_2^{ss}/CH_3^{ss} of approximately 0.7. The gradual increase in CH_2^{ss}/CH_3^{ss} indicates a rising *gauche*-defect density with increasing local pressure. A direct comparison of the vibrational amplitude changes discussed for the pressure dependent measurements with the results presented here is only possible to a limited extent: intensities analyzed here do not take the observed red shift of CH_3^{ss} or the different bandwidths of the two vibrations into account.

At 20 N, CH_2^{ss}/CH_3^{ss} changes only by a factor of approximately 1.5 between the pristine SAM and the contact center (Figure 7a) indicating that the pressure distribution with a maximum local pressure of 110 MPa applied is not sufficient to generate a large number of *gauche*-defects. This is well in line with the stress-dependent analysis, which shows that *gauche*-defect density increases strongly until a local pressure of ~155 MPa is reached. A comparison of Hertzian pressure distribution with the experimentally (*y*-scan of CH_2^{ss}/CH_3^{ss}) determined extent of the mechanical contact shows good agreement for all normal forces in Figure 7a–c, thus validating our measurements.

The spatial dependence of $l_{z,CH2}$, $l_{z,CH3}$, and the dihedral angle φ_{dih} under pressure in the MD simulations is shown by their radial distributions, which allow local effects to be detected on an atomistic level. Figure 8a shows this radial

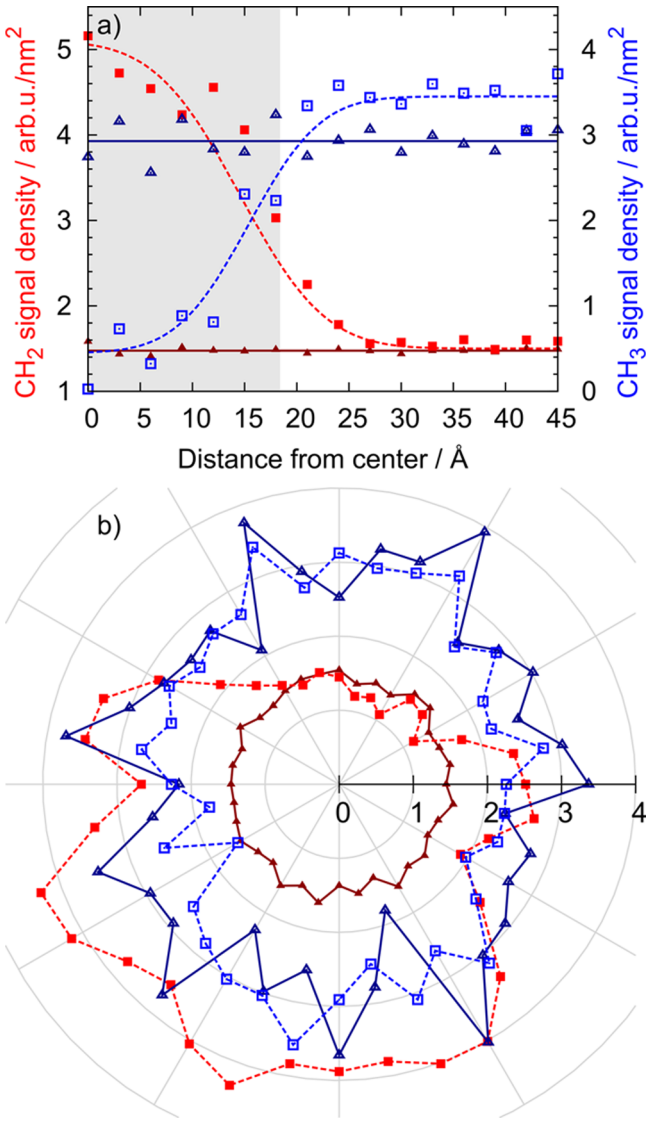

Figure 8. Average *z*-component of unperturbed $MD^{pristine}_{3.80/nm^2}$ (triangles) and perturbed $MD^{200\ MPa}_{3.80/nm^2}$ (squares) SAM for the CH_3 (open symbols) and CH_2 (filled symbols) bond vectors for the MD simulations, versus the radius from the center of interaction (a) and as polar plot versus the angle (b). The contact area is depicted as gray shaded area in (a).

distribution of the *z*-component of the CH_3 and CH_2 bond vectors for simulations $MD^{pristine}_{3.80/nm^2}$ and $MD^{200\ MPa}_{3.80/nm^2}$. As expected, the deviation from the value of a pristine SAM is largest in the contact center and weakens toward the rim, in good qualitative agreement with experimental findings. The effect is comparable for all the stressed systems, since the diameters of the contact areas are approximately equal and the CH_3 and CH_2 groups are all affected due to their close proximity to the simulated probe.

dx.doi.org/10.1021/ja5048076 | J. Am. Chem. Soc. 2014, 136, 10718–10727

A comparison of the contact area diameter (gray area in Figure 8a) and the radial change of $l_{z,CH2}$ and $l_{z,CH3}$ shows that stress-induced defects are also generated outside of the contact area up to a distance from the edge of the contact area of approximately 0.7 nm. This can be attributed to increased tilts in the molecules adjacent to those within the contact area. In the experiment this effect cannot be observed due to the limited spatial resolution of ∼100 μm. Another interesting finding is that the curve does not just level out for high radii in systems with low molecule density, but actually exceeds the base value. This phenomenon can most likely be attributed to the molecules below the sphere drawing aside and thus pressing the neighboring molecules into a less tilted configuration. This effect is not visible for the dense SAMs, owing to the fact that the tilt angle in this system is already very low (Supporting Information).

In combination with the experimental results we can now directly relate changes in the SFG spectra to structural changes which we observe in our microscopic simulations. Major structural changes are thus caused by the formation of *gauche*-defects in the SAM and are found in arbitrary positions of individual molecules. This result differs from previous simulations of compressed SAMs with different anchor groups than used in our study performed on diamond[22] and gold[64] substrates. In these studies, the initial and dominant response of SAMs to pressure is attributed to both an initial increase in tilt angles and an increase in *gauche*-defects, which are predominantly formed close to the molecular headgroup. These results were, however, obtained for flat or planar potentials with periodic boundary conditions. In contrast, our simulations are based on a spherical potential smaller than the simulated cell. Thus, not all molecules are directly affected by the applied position-dependent potential. We point out that our approach is much closer to the experiments performed in this study.

Another interesting result is that *gauche*-defect formation is not symmetric relative to the center of interaction for the lower-density systems. From Figure 8b, it can be clearly seen that the increase in CH_2 bond vector *z*-component mainly spreads in a distinct direction approximately opposite to the main tilt direction of a pristine SAM. The effect is also reflected in the anisotropy of the angular distribution of dihedral angles (Supporting Information). Due to the curvature of the interacting potential sphere, the potential acts in the tilt direction of the molecules on the one side and against the tilt on the other side of the contact center (Figure 1). When the forces act in the tilt direction, the molecules are more likely to increase their tilt, rather than forming *gauche*-defects. Thus, acting against the tilt obviously results in a higher *gauche*-defect density. The effect is also visible in Figure 3, where kinks and twists, color-coded with green and red, are mostly located in the left part of the snapshot. The higher the general tilt of the SAM, the more pronounced this effect is. From the conclusions above, it is clear that the anisotropy is also highly dependent on the curvature of the lens and thus the pressure gradient within the contact region. To observe this anisotropy experimentally a lateral resolution below the typical domain size of below 10 nm[65−67] would be required, which is far below the actual focus size (∼100 μm) of the laser beams in our SFG spectrometer. The direct correlation between the anisotropic distribution of *gauche* defects in system $MD^{200\ MPa}_{3.80/nm^2}$ and the corresponding anisotropic increase in CH_2 signal density, however, shows that it is indeed the *gauche* defects rather than the increased tilt that causes the change in signal intensity.

At this point we need to stress that the comparability between the experiments and the simulations is limited. The main and obvious reason is the difference in system size by several orders of magnitude which rules out a quantitative comparison. Nevertheless, we think that the model from our simulations fit the experimental system better than using a flat potential, since previous studies on pressurizing SAMs with flat surfaces,[22,23] as well as our own simulations, did not show the amount of gauche defect formation necessary to explain the increase in CH_2 signals in our SFG spectra. Considering the fact that in our experiments the surfaces of substrate (0.24 nm rms) and indenter (0.37 nm rms) are not perfectly smooth, we already have local pressure variations on a small nanometer scale which makes the comparison relevant. In addition, the work of Brenner et al. [23] nicely shows that even small asperities can have a substantial effect on the resulting pressure induced deformations in a SAM.

■ CONCLUSION

The indentation of self-assembled octadecylphosphonic acid (ODPA) monolayers on α-Al_2O_3(0001) has been studied in detail by *in situ* vibrational sum-frequency generation (SFG) and molecular-dynamics (MD) simulations. We provide clear evidence that indentation leads to the generation of two types of *gauche*-defects.

Laterally resolved studies of the contact area reveal a gradual increase of *gauche*-defect density from the edge of the contact area saturating close to the center. Comparison with Hertzian contact theory shows good agreement between the theoretically predicted and the experimentally determined sizes of the circular contact area and allows for a validation of our experiments. In full agreement with MD simulations, SFG spectra show negligible differences of pristine and relaxed ODPA SAMs after stress is released, which indicates complete reversibility of induced defects on an ultrafast time scale.

The combination of experimental and simulation studies has thus demonstrated reversible *gauche*-defect formation as a molecular self-healing mechanism that accounts for considerable resistance of the SAM toward mechanical stress.

■ ASSOCIATED CONTENT

Supporting Information

Details on the principles of sum-frequency generation, the Hertzian contact theory, the sample preparation procedures, the experimental details as well as details on the MD simulations, additional data from the simulated systems and on the relaxation are provided. This material is free of charge via the Internet at http://pubs.acs.org.

■ AUTHOR INFORMATION

Corresponding Author

*E-mail: wolfgang.peukert@fau.de

Present Address

¶Department of Chemical and Environmental Engineering, University of Nottingham, University Park Nottingham NG7 2RD.

Author Contributions

Christian Meltzer and Jonas Paul have contributed equally to this publication.

Notes

The authors declare no competing financial interest.

■ ACKNOWLEDGMENTS

The authors gratefully acknowledge funding by the German National Science Foundation (DFG) through the priority program "Particles in Contact", Project No. PE427/19-2 and the GRK 1896 "In-Situ microscopy with Electrons, X-rays and Scanning Probes", the support by the Cluster of Excellence "Engineering of Advanced Materials" and the Erlangen Graduate School in Advanced Optical Technologies (SAOT) at the Friedrich-Alexander-Universität Erlangen-Nürnberg (FAU), within the framework of the "Excellence Initiative".

■ REFERENCES

(1) Chaki, N. K.; Vijayamohanan, K. *Biosens. Bioelectron.* **2002**, *17*, 1.
(2) Lin, Y.-Y.; Gundlach, D. J.; Nelson, S. F.; Jackson, T. N. *IEEE Trans. Electron Devices* **1997**, *44*, 1325.
(3) Laibinis, P. E.; Whitesides, G. M. *J. Am. Chem. Soc.* **1992**, *114*, 9022.
(4) Tambe, N. S.; Bhushan, B. *Nanotechnology* **2005**, *16*, 1549.
(5) Prime, K. L.; Whitesides, G. M. *Science* **1991**, *252*, 1164.
(6) Rumpel, A.; Novak, M.; Walter, J.; Braunschweig, B.; Halik, M.; Peukert, W. *Langmuir* **2011**, *27*, 15016.
(7) Novak, M.; Ebel, A.; Meyer-Friedrichsen, T.; Jedaa, A.; Vieweg, B. F.; Yang, G.; Voitchovsky, K.; Stellacci, F.; Spiecker, E.; Hirsch, A.; Halik, M. *Nano Lett.* **2011**, *11*, 156.
(8) Schickle, K.; Korsten, A.; Weber, M.; Bergmann, C.; Neuss, S.; Fischer, H. *J. Eur. Ceram. Soc.* **2013**, *33*, 2705.
(9) Seitz, O.; Böcking, T.; Salomon, A.; Gooding, J. J.; Cahen, D. *Langmuir* **2006**, *22*, 6915.
(10) Claridge, S. A.; Liao, W.-S.; Thomas, J. C.; Zhao, Y.; Cao, H. H.; Cheunkar, S.; Serino, A. C.; Andrews, A. M.; Weiss, P. S. *Chem. Soc. Rev.* **2013**, *42*, 2725.
(11) Cheng, H.; Hu, Y. *Adv. Colloid Interface Sci.* **2012**, *171*−*172*, 53.
(12) McCarthy, F. J.; Buck, M.; Hähner, G. *J. Phys. Chem. C* **2008**, *112*, 19465.
(13) Perry, S. S.; Lee, S.; Shon, Y.-S.; Colorado, R., JR.; Lee, T. R. *Tribol. Lett.* **2001**, *10*, 81.
(14) Cui, B.; Zhang, L.; Zhou, H.; Zhang, J.; Chen, J. *Surf. Interface Anal.* **2011**, *43*, 1377.
(15) Qian, L.; Charlot, M.; Perez, E.; Luengo, G.; Potter, A.; Cazeneuve, C. *J. Phys. Chem. B* **2004**, *108*, 18608.
(16) Yu, J.; Banquy, X.; Greene, G. W.; Lowrey, D. D.; Israelachvili, J. N. *Langmuir* **2012**, *28*, 2244.
(17) Bhushan, B.; Israelachvili, J. N.; Landman, U. *Nature* **1995**, *374*, 607.
(18) Glosli, J. N.; McClelland, G. M. *Phys. Rev. Lett.* **1993**, *70*, 1960.
(19) Koike, A.; Yoneya, M. *J. Phys. Chem. B* **1998**, *102*, 3669.
(20) Tupper, K. J.; Brenner, D. W. *Thin Solid Films* **1994**, *253*, 185.
(21) Chandross, M.; Lorenz, C. D.; Stevens, M. J.; Grest, G. S. *Langmuir* **2008**, *24*, 1240.
(22) Tutein, A. B.; Stuart, S. J.; Harrison, J. A. *Langmuir* **2000**, *16*, 291.
(23) Tupper, K. J.; Colton, R. J.; Brenner, D. W. *Langmuir* **1994**, *10*, 2041.
(24) Harrison, J. A.; Gao, G. T.; Chateauneuf, G. M.; David Schall, J.; van Workum, K.; Mikulski, P. T. *Proc. World Tribol. Cong.* **2005**, 707.
(25) Eisert, F.; Gurka, M.; Legant, A.; Buck, M.; Grunze, M. *Science* **2000**, *287*, 468.
(26) Beattie, D. A.; Haydock, S.; Bain, C. D. *Vib. Spectrosc.* **2000**, *24*, 109.
(27) Nanjundiah, K.; Hsu, P. Y.; Dhinojwala, A. *J. Chem. Phys.* **2009**, *130*, 24702.
(28) Fraenkel, R.; Butterworth, G. E.; Bain, C. D. *J. Am. Chem. Soc.* **1998**, *120*, 203.
(29) Beattie, D. A.; Fraenkel, R.; Winget, S. A.; Petersen, A.; Bain, C. D. *J. Phys. Chem. B* **2006**, *110*, 2278.
(30) Berg, O.; Klenerman, D. *J. Am. Chem. Soc.* **2003**, *125*, 5493.
(31) Berg, O.; Klenerman, D. *J. Appl. Phys.* **2001**, *90*, 5070.
(32) Du, Q.; Xiao, X.-D.; Charych, D.; Wolf, F.; Frantz, P.; Shen, Y. R.; Salmeron, M. *Phys. Rev. B* **1995**, *51*, 7456.
(33) Ghalgaoui, A.; Shimizu, R.; Hosseinpour, S.; Álvarez-Asencio, R.; McKee, C.; Johnson, C. M.; Rutland, M. W. *Langmuir* **2014**, *30*, 3075.
(34) Lagutchev, A. S.; Patterson, J. E.; Huang, W.; Dlott, D. D. *J. Phys. Chem. B* **2005**, *109*, 5033.
(35) Patterson, J. E.; Dlott, D. D. *J. Phys. Chem. B* **2005**, *109*, 5045.
(36) Huang, W.; Patterson, J. E.; Lagutchev, A.; Dlott, D. D. *AIP Conf. Proc.* **2006**, *845*, 1265.
(37) Lambert, A. G.; Davies, P. B.; Neivandt, D. J. *Appl. Spectrosc. Rev.* **2005**, *40*, 103.
(38) Zhang, L.; Tian, C.; Waychunas, G. A.; Shen, Y. R. *J. Am. Chem. Soc.* **2008**, *130*, 7686.
(39) Brukman, M. J.; Marco, G. O.; Dunbar, T. D.; Boardman, L. D.; Carpick, R. W. *Langmuir* **2006**, *22*, 3988.
(40) Thissen, P.; Valtiner, M.; Grundmeier, G. *Langmuir* **2010**, *26*, 156.
(41) Greenwood, J.; Tripp, J. *J. Appl. Mech.* **1967**, 153.
(42) Jäger, C. M.; Schmaltz, T.; Novak, M.; Khassanov, A.; Vorobiev, A.; Hennemann, M.; Krause, A.; Dietrich, H.; Zahn, D.; Hirsch, A.; Halik, M.; Clark, T. *J. Am. Chem. Soc.* **2013**, *135*, 4893.
(43) Bauer, T.; Schmaltz, T.; Lenz, T.; Halik, M.; Meyer, B.; Clark, T. *ACS Appl. Mater. Interfaces* **2013**, *5*, 6073.
(44) Hauffman, T.; Blajiev, O.; Snauwaert, J.; Haesendonck, C. V.; Hubin, A.; Terryn, H. *Langmuir* **2008**, *24*, 13450.
(45) Liakos, I. L.; Newman, R. C.; McAlpine, E.; Alexander, M. R. *Surf. Interface Anal.* **2004**, *36*, 347.
(46) Luschtinetz, R.; Oliveira, A. F.; Duarte, H. A.; Seifert, G. *Z. Anorg. Allg. Chem.* **2010**, *636*, 1506.
(47) Wang, J.; Wolf, R. M.; Caldwell, J. W.; Kollman, P. A.; Case, D. A. *J. Comput. Chem.* **2004**, *25*, 1157.
(48) Sun, J.; Stirner, T.; Hagston, W. E.; Leyland, A.; Matthews, A. *J. Cryst. Growth* **2006**, *290*, 235.
(49) Smith, W.; Forester, T. R.; Todorov, I. T. *The DL_POLY Classic User Manual*; STFC Daresbury Laboratory: Daresbury, U.K.
(50) DL_POLY Classic Molecular Dynamics Simulation Package; http://www.ccp5.ac.uk/DL_POLY_CLASSIC/.
(51) Berendsen, H. J. C.; Postma, J. P. M.; van Gunsteren, W. F.; Dinola, A.; Haak, J. R. *J. Chem. Phys.* **1984**, *81*, 3684.
(52) Nishi, N.; Hobara, D.; Yamamoto, M.; Kakiuchi, T. *J. Chem. Phys.* **2003**, *118*, 1904.
(53) Novak, M.; Jäger, C. M.; Rumpel, A.; Kropp, H.; Peukert, W.; Clark, T.; Halik, M. *Org. Electron.* **2010**, *11*, 1476.
(54) Guyot-Sionnest, P.; Hunt, J. H.; Shen, Y. R. *Phys. Rev. Lett.* **1987**, *59*, 1597.
(55) Tyrode, E.; Hedberg, J. *J. Phys. Chem. C* **2012**, *116*, 1080.
(56) Ward, R. N.; Duffy, D. C.; Davies, P. B.; Bain, C. D. *J. Phys. Chem.* **1994**, *98*, 8536.
(57) Spori, D. M.; Venkataraman, N. V.; Tosatti, S. G. P.; Durmaz, F.; Spencer, N. D.; Zürcher, S. *Langmuir* **2007**, *23*, 8053.
(58) Lu, R.; Gan, W.; Wu, B.-H.; Zhang, Z.; Guo, Y.; Wang, H.-F. *J. Phys. Chem. B* **2005**, *109*, 14118.
(59) Bell, G. R.; Bain, C. D.; Ward, R. N. *J. Chem. Soc., Faraday Trans.* **1996**, *92*, 515.
(60) Conboy, J. C.; Messmer, M. C.; Richmond, G. L. *J. Phys. Chem. B* **1997**, *101*, 6724.
(61) Stole, S. M.; Porter, M. D. *Langmuir* **1990**, *6*, 1199.
(62) Ong, T. H.; Davies, P. B.; Bain, C. D. *Langmuir* **1993**, *9*, 1836.
(63) Wang, Z.; Mohammadzadeh, S.; Schmaltz, T.; Kirschner, J.; Khassanov, A.; Eigler, S.; Mundloch, U.; Backes, C.; Steinrück, H.-G.; Magerl, A.; Hauke, F.; Hirsch, A.; Halik, M. *ACS Nano* **2013**, *7*, 11427.
(64) Ramin, L.; Jabbarzadeh, A. *Modell. Simul. Mater. Sci. Eng.* **2012**, *20*, 85010.
(65) Siepmann, J. I.; McDonald, I. R. *Langmuir* **1993**, *9*, 2251.
(66) Tidswell, I. M.; Rabedeau, T. A.; Pershan, P. S.; Kosowsky, S. D.; Folkers, J. P.; Whitesides, G. M. *J. Chem. Phys.* **1991**, *95*, 2854.
(67) Baptiste, A.; Gibaud, A.; Bardeau, J. F.; Wen, K.; Maoz, R.; Sagiv, J.; Ocko, B. M. *Langmuir* **2002**, *18*, 3916.